Journal of the Optical Society of America B
OPTICAL PHYSICS

Thin-film lithium niobate modulators for non-invasive sensing of high-frequency electric fields

JOHN ROLLINSON,[1,*] MONA HELLA,[1] SEYFOLLAH TOROGHI,[2] PAYAM RABIEI,[2] AND INGRID WILKE[3]

[1]Department of Electrical and Computer Systems Engineering, Rensselaer Polytechnic Institute, 110 8th Street, Troy, New York 12180, USA
[2]Partow Technologies, LLC, 1487 Poinsettia Ave., Suite 119 Vista, California 92081, USA
[3]Department of Physics, Applied Physics, and Astronomy, Rensselaer Polytechnic Institute, 110 8th Street, Troy, New York 12180, USA
*Corresponding author: rollij2@rpi.edu

Received 16 October 2020; revised 3 December 2020; accepted 8 December 2020; posted 9 December 2020 (Doc. ID 412758); published 4 January 2021

We propose a non-invasive, large-bandwidth electro-optic (EO) detection scheme for high-frequency electric fields using thin-film lithium niobate Mach–Zehnder interferometers. Our proof-of-concept device is capable of detecting high-strength electric fields, such as those present in x-ray free electron lasers and linear accelerators. The proposed detection scheme utilizes an off-the-shelf C-band fiber optic continuous-wave laser and optical spectrum analyzer, which has a lower system cost and footprint compared to bulk-crystal-based schemes. Towards this objective, fabricated devices are characterized in the 1–40 GHz frequency range to estimate the detection threshold, detection bandwidth, and EO modulation strength. The characterized device exhibits a $0.13\,\mathrm{V}\cdot\mathrm{m}^{-1}\cdot\mathrm{Hz}^{-1/2}$ normalized electric field sensitivity. By extrapolating the measured frequency response, it is expected that the characterized device will be able to detect free-space electric fields up to 150 GHz.

https://doi.org/10.1364/JOSAB.412758

1. INTRODUCTION

The sensing of high-frequency (millimeter-wave and above) electric fields in free space is a challenging task requiring sensitive, non-invasive detectors with high spatial and temporal resolution [1–3]. Standard antenna-based schemes for characterizing high-frequency electric fields are inherently limited in their temporal resolution by the bandwidth of the associated electronics, limited in their spatial resolution by the detector size, and can distort electric fields due to the presence of metallic components, requiring precise compensation [2,4]. Electro-optic (EO) sensing modalities address many of these limitations (Fig. 1). The linear EO effect occurs in non-centrosymmetric crystals, wherein an applied electric field modifies the refractive index of the material, producing polarization and phase modulation, also known as the Pockels effect [5]. The EO effect occurs effectively instantaneously, enabling high temporal resolution. Additionally, all-dielectric EO sensors produce negligible distortion of the sampled electric field. The sensitivity is dependent upon the Pockels coefficient of the EO crystal and the efficiency of the fabricated modulator [5].

In this work, we propose to apply advances in thin-film lithium-niobate-on-insulator (LNOI) modulator technology to develop non-invasive, large-bandwidth, and high-sensitivity EO electric field sensors. As a proof-of-principle demonstration, LNOI Mach–Zehnder interferometers (MZIs) are fabricated and characterized in the range of 1–40 GHz (limited by available equipment) to determine the device's phase modulation coefficient, minimum detection threshold, and estimated detection bandwidth. In our detection scheme (Fig. 1), electric fields incident upon an integrated LN MZI produce amplitude modulation in a continuous-wave (CW) probe laser. This modulation produces optical sidebands in the frequency domain measured via an optical spectrum analyzer (OSA). Since the MZI is the basic building block of optical vector analysis (OVA) [6,7], phase-sensitive detection of the high-frequency electric field is thus possible, though not yet developed in this work. With both amplitude- and phase-spectrum information, the time-domain signal can then be reconstructed via an inverse Fourier transform, and the temporal resolution of the reconstructed signal is thus limited by the detection bandwidth of the EO modulator (i.e., $t_s = 1/f_s$, where f_s is equivalent to the detection bandwidth). Thin-film LNOI technology has the potential to advance OVA towards chip-based instruments with increased bandwidth because the detection scheme can be applied to sample high-frequency electric fields using

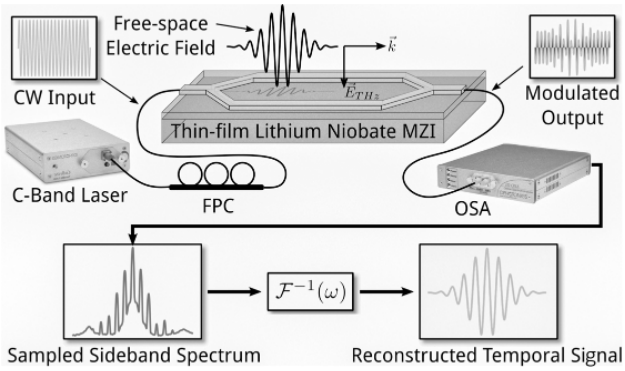

Fig. 1. Frequency-domain electro-optic detection scheme. Incident electric fields produce phase and amplitude modulation in an optical probe beam, which is captured in the frequency domain using an OSA.

off-the-shelf C-band telecommunications equipment to reduce system cost, footprint, and complexity and increase robustness.

While the scheme presented here is one possible method of achieving integrated, frequency-domain EO electric field sampling, an alternative scheme could be realized by more closely mimicking prior free-space, femtosecond-pulsed-laser-based schemes [8,9]. Using thin-film LN, the bulk EO crystal can be replaced by a thin-film LN waveguide wire sensor [10], the quarter-wave plate by a thin-film MZI, and the Wollaston prism by an integrated TE/TM mode splitter [11]. Integrated tunable optical delay lines have also been demonstrated [12], though not in thin-film LN. Thus, thin-film LNOI technology has the potential for chip-scale integration of a femtosecond-pulsed laser EO detection scheme.

EO measurement schemes are important in fields such as plasma physics, accelerator science, biomedical sensing, laser radar, and microwave integrated circuit and antenna characterization [13–18]. Prior EO detection schemes have utilized bulk EO crystals [8]. The sensitivity and bandwidth of such detectors are limited by the phase mismatch (related directly to the refractive index mismatch) between the optical and RF electric fields within the EO crystal. LN ($LiNbO_3$) is one such EO crystal that exhibits strong linear EO modulation ($r_{33} = 30.8$ pm/V) and transparency at near-infrared wavelengths [5]. Bulk LN, however, exhibits an unfavorably high phase mismatch at terahertz and sub-terahertz frequencies ($\Delta n = n_{\mathrm{RF}} - n_{\mathrm{opt}} = 4.39$ for $f_{\mathrm{RF}} = 100$ GHz and $\lambda_{\mathrm{opt}} = 1550$ nm) [19], yielding poor signal-to-noise ratios (SNRs) when used in terahertz EO detection schemes [8]. Field sensitivities as low as $1\ \mathrm{V} \cdot \mathrm{m}^{-1} \cdot \mathrm{Hz}^{-1/2}$ have been demonstrated, but bandwidths in LN detectors have been limited to less than 20 GHz due to the inherent phase mismatch of bulk LN [18]. For EO sampling at frequencies above 100 GHz, ZnTe and GaP offer much larger bandwidths (ZnTe: $f_c \sim 3$ THz; GaP: $f_c \sim 7$ THz) but are limited in sensitivity by lower EO coefficients than LN (ZnTe: $r_{41} = 3.90$ pm/V; GaP: $r_{41} = 0.97$ pm/V) [9].

The advent of crystal ion slicing (CIS) and thermal exfoliation techniques enabling the fabrication of inexpensive thin-film LNOI wafers has paved the way for renewed interest in LN for building compact, high-efficiency, large-bandwidth integrated optical modulators for applications in fiber optic communications [20]. The high index contrast of LNOI waveguides results in dramatically improved mode confinement over bulk devices, leading to improved EO modulation strength, reduced modulator length, and reduced bending radii. Recently, researchers have demonstrated higher modulation bandwidths and CMOS-compatible operating voltages on LNOI platforms [21–25]. Most importantly, phase matching of the RF and optical fields has been achieved through engineering of waveguide cladding layers, overcoming a fundamental limitation of bulk LN to extend experimental modulator bandwidths to 500 GHz, with 1 THz achievable bandwidth being projected [26]. While MZI modulators with very high bandwidth have been demonstrated, in this work, it is not our intent to compete with these state-of-the-art modulators, but rather to demonstrate an alternative application. Note that, rather than referring the commonly used 3 dB modulation bandwidth, here we define the *detection* bandwidth as the frequency range over which the first sideband (FSB) can be measured with >3 dB optical SNR (OSNR), as this metric is more relevant to frequency-domain electric field detection. This parameter is thus subject to experimental conditions (e.g., electric field strength, noise floor, dynamic range, etc.).

2. DEVICE PRINCIPLES AND DESIGN

Thin-film LN modulator technology [27] is considered a key enabling technology for non-invasive EO sensing of AC electric fields with terahertz frequency bandwidth. Using thin-film LN, it is possible to perfectly phase match the terahertz wave signal and the optical signal by engineering the optical waveguide. An MZI is chosen rather than a simpler single-waveguide phase modulator to distinguish phase modulation due to the electric field from any phase modulation due to environmental factors (e.g., vibrations, thermal fluctuations).

The modulator consists of an input and an output grating coupler to couple light between optical fibers and the thin-film modulator devices and a Mach–Zehnder modulator section where two arms are used [Fig. 2(a)]. A fiber v-groove array is

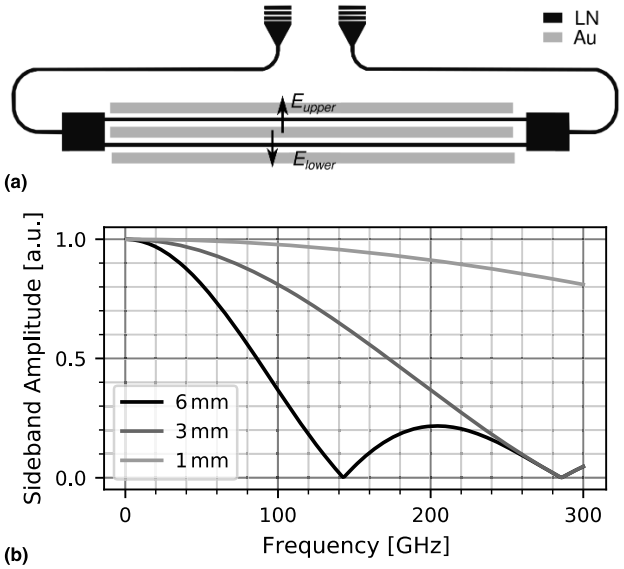

Fig. 2. (a) Schematic of the modulator device and (b) calculated modulation bandwidth for thin-film LN modulators with different MZI device arms lengths. $n_{\mathrm{opt}} = 2.3$, $n_{\mathrm{RF}} = 1.95$.

Table 1. Technical Specifications of the MZI Modulator Used in This Research

Parameter	Value
Operating wavelength	1550 nm
Fiber-to-fiber insertion loss	−14 to −17 dB
Optical return loss	>40 dB
Extinction ratio	>20 dB
3 dB Bandwidth	50 GHz
V_π (DC)	6.5 V
Active electrode length	6 mm
RF transmission line impedance	50 Ω

aligned and attached to the modulator to couple light in and out of the device. The fabrication process is described in detail in Ref. [27]. The measured device parameters are summarized in Table 1. The electric field is reversed for one MZI arm compared to the second arm using coplanar RF waveguides. The normalized modulation index (independent of electric field strength) as a function of RF for the thin-film LN modulator is given by (1), where α is the RF loss parameter; L is the EO interaction length; n_{RF} and n_{opt} are the effective RF and optical refractive indices, respectively; and ω_{RF} is the modulating frequency [20]. Equation (1) is plotted in Fig. 2(b) for three different device lengths:

$$\delta_{\mathrm{norm}} = \sqrt{\frac{\sinh\left(\frac{\alpha L}{2}\right)^2 + \sin\left(\left(n_{\mathrm{RF}} - n_{\mathrm{opt}}\right)\frac{\omega_{\mathrm{RF}} L}{2c}\right)^2}{\left(\frac{\alpha L}{2}\right)^2 + \left(\left(n_{\mathrm{RF}} - n_{\mathrm{opt}}\right)\frac{\omega_{\mathrm{RF}} L}{2c}\right)^2}}. \quad (1)$$

The effect of RF and optical index mismatch ($\Delta n = n_{\mathrm{RF}} - n_{\mathrm{opt}}$) on the device's detection bandwidth can be directly understood from (1). In the ideal case of no electrical losses ($\alpha = 0$), as Δn approaches zero, δ_{norm} approaches unity. Thus, the index mismatch must be minimized to maximize the detection bandwidth, through tuning the waveguide geometry to adjust n_{opt} [20], the addition of cladding layers to adjust n_{RF} [26], or tuning the substrate (typically SiO_2) thickness to adjust n_{RF} [28]. Inherently, maximizing δ_{norm} by minimizing Δn will also maximize the device sensitivity, and thus the OSNR and the detection bandwidth are simultaneously improved by reducing the index mismatch [5]. The reduction of this mismatch is limited partly by the difficulty of fabricating thin-film LN devices, although fabrication methods are being continuously improved upon, and successful wafer-scale fabrication of integrated LN devices has recently been demonstrated [29].

The group refractive index for the optical mode in these devices is equal to 2.3. The group refractive index for the traveling terahertz wave is not affected by sub-micrometer LN thin films and is approximately equal to 1.95 (i.e., the refractive index of SiO_2) at terahertz frequencies. In these devices, a 300 nm SiN ridge is patterned on a 300 nm thin LN thin-film layer. Note that because this work is intended only as a proof-of-principle demonstration, a readily available LN MZI is used rather than one specifically optimized for this application. Further increase in the device bandwidth is readily possible by designing the waveguide structure to achieve better phase matching or simply by using shorter interaction lengths [Fig. 2(b)]. The group refractive index of the optical mode can be engineered to be in the 1.8–2.3 range depending on waveguide dimensions at a laser wavelength of 1550 nm. Hence, in theory, it is possible to perfectly phase match the terahertz signal and the optical signal in thin-film LN waveguide modulators. If free-space terahertz wave signals are used for modulation, one arm can be poled to reverse the direction of spontaneous polarization of LN crystal to achieve an opposite refractive index change for the same electric field and hence achieve intensity modulation in the output for sensing applications [30].

3. EXPERIMENTAL DESIGN

Device characterization is performed using a setup similar to Fig. 1. An RF signal generator (Anritsu 68369a/nv) with 40 GHz bandwidth is used to apply RF signals to the coplanar transmission line of the MZI to emulate free-space electric fields. An RF amplifier (Mini Circuits ZVA-213-S+) boosts the maximum power to 24 dBm at 10 GHz. Gain flattening is applied to maintain a constant 20 dBm output power across the characterization bandwidth. A bias tee is used to adjust the DC bias point of the MZI to optimize its sensitivity.

The optical elements consist of a tunable CW C-band laser (Pure Photonics PPCL100, $P_{\mathrm{max}} = 13.5$ dBm) operated at 1550 nm (193.5 THz), a manual paddle-style fiber polarization controller (FPC) (ThorLabs FPC560), the MZI device under test, and a C-band OSA (ID-Photonics ID-OSA-MPD-00). The laser beam is polarized parallel to the optic axis of the LN modulator with a 35 dB polarization extinction ratio (PER), tuned using the manufacturer-specified polarization tuning procedure [31]. The OSA operates with a 312.5 MHz sampling resolution, a 1.7 GHz resolution bandwidth, and a 1 Hz scan rate.

4. EXPERIMENTAL RESULTS

Characterization is focused primarily on determining the device bandwidth and absolute electric field sensitivity, the parameters relevant to high-frequency electric field sensing. Under maximum available RF and optical power, excellent sideband generation in the 1–40 GHz range is observed. Five detectable sidebands are generated using $f_{\mathrm{RF}} = 10$ GHz and $P_{\mathrm{RF}} = 24$ dBm. Based on MZI device theory, the nth sideband amplitude is given as $P_n = P_0 \cdot J_n(\delta)^2$, where P_0 is the optical probe power, J_n is the n th-order Bessel function, and δ is the modulation index, which depends on the RF and optical field intensities, the Pockels coefficient, effective refractive index of LN, and device geometry (electrode spacing, mode confinement, RF/optical field overlap, etc.) [5]. Figure 3 compares experimentally measured sideband amplitude with theoretical predictions at 10 GHz and 15 GHz, respectively. Both the frequency and amplitude of the sidebands agree well with expectations, within the limits of simulation accuracy. Note that, because this experiment is intended only as a proof of principle, the simulation used here is an analytical model based on established device theory [5] and tabulated material data, and thus does not predict the experimental results as accurately as a device-level simulation would. In general, model agreement is good, given that non-ideal aspects such as losses and process

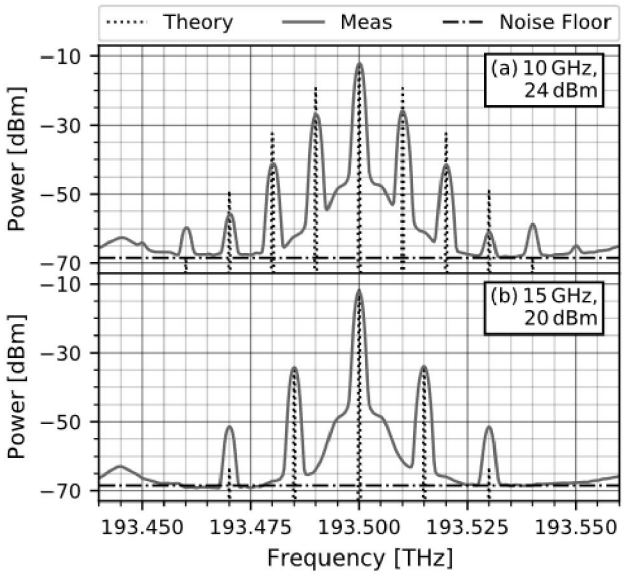

Fig. 3. Optical sideband spectra for (a) $f_{RF} = 10$ GHz, $P_{RF} = 24$ dBm and (b) $f_{RF} = 15$ GHz, $P_{RF} = 20$ dBm. The elevated noise floor at the edges of the plot is due to the suppressed side modes of the laser (PPCL100). Note that the power level in (a) is 24 dBm, and hence the sideband ratios in this plot do not correspond to those in Fig. 5.

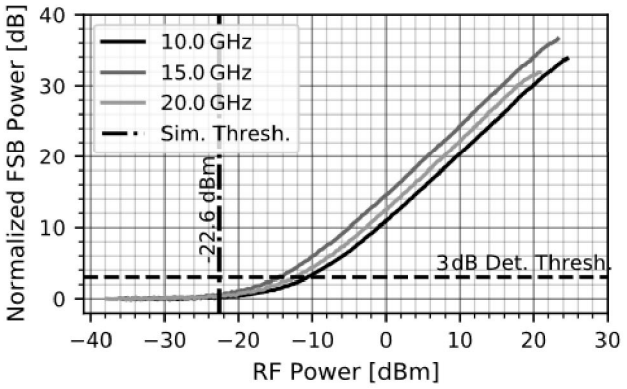

Fig. 4. RF power dependence of first sideband amplitude at 10, 15, and 20 GHz. A −22.6 dBm detection threshold is expected from numerical simulations at 10 GHz. Note that at 10 GHz, detection of the first sideband is limited by the increased detection threshold due to the laser profile (see Fig. 5).

effects are not included. In both cases, sideband generation is stronger than expected from theory for higher-order sidebands and more sidebands are observed than predicted. Because the RF amplifier is operated near the point of saturation, this increased sideband amplitude is attributable to harmonic distortion of the amplified modulation signal.

The threshold RF power to produce detectable sidebands is measured by sweeping RF power at three frequencies (10, 15, and 20 GHz). A detectable sideband is defined as a sideband with an OSNR greater than 3 dB (with −70 dBm noise floor). Figure 4 shows the results of this characterization. The device shows good RF power sensitivity; power levels as low as −14.4 dBm at 15 GHz produce reliable sideband detection

Table 2. RF Power Detection Thresholds and Corresponding Estimated Incident Electric Field

Frequency (GHz)	Min. Power (dBm)	E-Field (kV/m)
10	−10.5	8.4
15	−14.4	5.4
20	−12.4	6.8

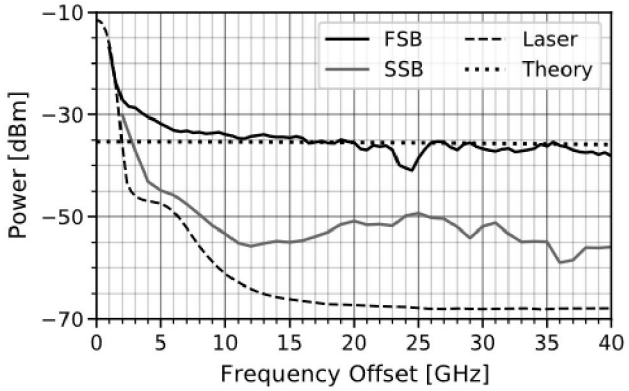

Fig. 5. FSB and SSB amplitudes measured over a 1–40 GHz RF modulation frequency range. Frequency offset refers to the separation between the sideband frequency and the probe light frequency (i.e., $f_n - f_0$, where $n = 1, 2$). The experimental data are fit with (1) and extrapolated to estimate a detection bandwidth of 150 GHz, in agreement with theoretical expectations. The laser linewidth profile (dashed line, - - -) is included to illustrate its effect on sideband detectability (relating to Fig. 4). FSB, first sideband; SSB, second sideband.

(Table 2). The RF electric field in the center of the LN waveguide is estimated from power measurements using a simple $E = V/d$ relationship for 7 μm electrode spacing, where the traveling-wave voltage on the electrodes is calculated from the applied power after accounting for electrical losses, assuming a 50 Ω transmission line. Table 2 lists the calculated electric field thresholds. The best-case E_{min} of 5.4 kV/m is observed at 15 GHz. After normalizing by the 1.7 GHz OSA resolution bandwidth, this corresponds to an electric field sensitivity of $0.13\ \mathrm{V \cdot m^{-1} \cdot Hz^{-1/2}}$.

To estimate the detection bandwidth of this device, the sideband amplitudes are measured while sweeping the RF modulation frequency from 1–40 GHz, at a constant 20 dBm RF power (Fig. 5). The experimental sideband frequency dependence is then fit with (1) and extrapolated to estimate the −70 dBm (noise floor) intercept. Using this method, the detection bandwidth is estimated to be 150 GHz, in good agreement with theory. Note that, while the device clearly possesses electrical losses that contribute to the attenuation of the sideband amplitude over this frequency range (Fig. 6), these losses have been intentionally removed in this fit. The electrical contacts and transmission line are included on this device only for characterization purposes. In a practical EO sensing scenario, the detector would not include metallic components as it would be measuring a free-space electric field (Fig. 1), and thus the only electrical losses would be due to absorption, which is expected to be negligible [19].

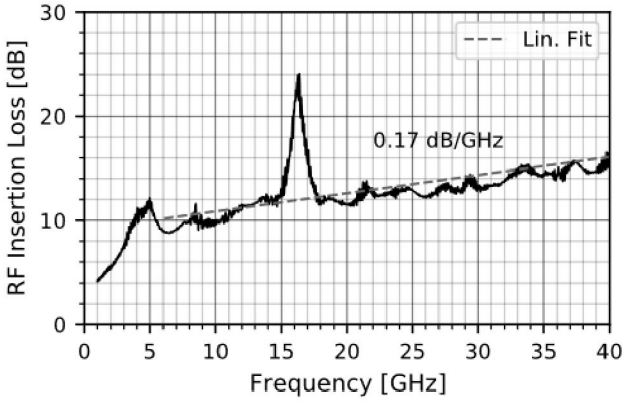

Fig. 6. RF insertion loss over the measured frequency range. Between 6 and 40 GHz, the range over which the insertion loss increases approximately linearly (with the exception of a sharp peak at 16 GHz), the insertion loss increases by 0.17 dB/GHz.

5. CONCLUSION

In this work, we propose a frequency-domain EO sampling scheme for the detection of high-frequency electric fields based on an integrated LN MZI. Thin-film LN MZIs are fabricated and characterized to assess their performance as high-frequency electric field sensors as a proof-of-principle demonstration. The detector is estimated to have a best-case electric field sensitivity of $0.13\ \mathrm{V}\cdot\mathrm{m}^{-1}\cdot\mathrm{Hz}^{-1/2}$. Based on extrapolation of experimental data, the device can be expected to detect free-space electric fields of this amplitude up to 150 GHz.

Based on the measured $E_{\min}$ and extrapolated detection bandwidth, this device would be suitable for measuring relatively high-intensity electric fields, such as those of accelerated electron bunches in x-ray free electron lasers (XFELs) and linear accelerators (LINACs). For example, at the European X-ray Free Electron Laser, the field in the vicinity (∼mm) of the 1 nC accelerated electron bunch is $E \approx 10^5\ \mathrm{V/m}$, and the bunch length varies along the beam line from 6.8 ps ($f = 1/T \approx 147$ GHz) (downstream from the injector LINAC) to 300 fs ($f = 1/T \approx 3$ THz) (following three bunch compression stages) [32]. Thus, the device would be suitable for measurement of the electron bunch length prior to the first compression stage. Given that the phase of the electric field of accelerated electron bunches is constant, no phase measurement scheme would be necessary, and conceptually, the temporal electric field profile can be reconstructed from the OSA measurement [14]. However, a higher detection bandwidth would be needed to resolve shorter electron bunches (i.e., after bunch compression).

The performance of this particular device as an electric field sensor is limited by a number of factors. $E_{\min}$ is limited by the refractive index mismatch of the device and the interaction length (6 mm). Minimizing this mismatch would significantly improve the sensitivity of the device. The device possesses an inherent sensitivity–bandwidth tradeoff, which scales linearly with 1/L (EO interaction length) (i.e., reducing the interaction length increases the bandwidth at the cost of increasing the $E_{\min}$). For example, reducing the device length to 0.9 mm would increase the bandwidth to 1 THz while increasing $E_{\min}$ to approximately 36 kV/m. Alternatively, as discussed previously, the index mismatch could be minimized through engineering of the waveguide and cladding layers to improve both the bandwidth and sensitivity. Additionally, the minimum detectable electric field is determined by the OSNR measured at the OSA, which is limited by the side-mode-suppression ratio (SMSR) and OSNR of the laser and the dynamic range of the OSA. The laser used in this work exhibits an OSNR/SMSR of approximately 50–60 dB (depending on output power) while the OSA is capable of up to 70 dB dynamic range. A 20 dB improvement in the system's OSNR (e.g., by increasing the laser's power while maintaining a −70 dBm noise floor) would correspond to an order-of-magnitude improvement in the minimum detectable electric field.

Funding. Small Business Innovation Research (DE-SC0019625, DE-FOA-0001940).

Acknowledgment. I. W. and Partow Technologies, LLC, conceived of the application and experimental design. P. R. and S. T. performed device design and fabrication. J.R. performed device characterization and manuscript preparation. I. W. and M. H contributed to discussions and interpretation of results, and supervised the project.

Disclosures. P. R. and S. T.: Partow Technologies, LLC (E).

REFERENCES

1. J. Peng, S. Jia, J. Bian, S. Zhang, J. Liu, and X. Zhou, "Recent progress on electromagnetic field measurement based on optical sensors," Sensors **19**, 2860 (2019).
2. A. Kainz, H. Steiner, J. Schalko, A. Jachimowicz, F. Kohl, M. Stifter, R. Beigelbeck, F. Keplinger, and W. Hortschitz, "Distortion-free measurement of electric field strength with a mems sensor," Nat. Electron. **1**, 68–73 (2018).
3. D. Hill and M. Kanda, *The Measurement, Instrumentation, and Sensors Handbook XXV* (CRC Press/IEEE, 1999).
4. H. Kirkham, "On the measurement of stationary electric fields in air," in *Conference of Precision Electromagnetic Measurements* (2002).
5. A. Yariv and P. Yeh, *Optical Waves in Crystals: Propagation and Control of Laser Radiation* (Wiley, 1984).
6. O. Morozov, I. Nureev, A. Sakhabutdinov, A. Kuznetsov, G. Morozov, G. Il'in, S. Papazyan, A. Ivanov, and R. Ponomarev, "Ultrahigh-resolution optical vector analyzers," Photonics **7**, 14 (2020).
7. S. Liu, M. Xue, J. Fu, L. Wu, and S. Pan, "Ultrahigh-resolution and wideband optical vector analysis for arbitrary responses," Opt. Lett. **43**, 727–730 (2018).
8. C. Winnewisser, P. U. Jupsen, M. Schall, V. Schyja, and H. Helm, "Electro-optic detection of THz radiation in $LiTaO_3$, $LiNbO_3$, and ZnTe," Appl. Phys. Lett. **70**, 3069 (1997).
9. I. Wilke and S. Sengupta, "Nonlinear optical techniques for terahertz pulse generation and detection—optical rectification and electrooptic sampling," in *Terahertz Spectroscopy: Principles and Applications*, S. L. Dexheimer, ed. (2007), Chap. 2.
10. G. Poberaj, H. Hu, W. Sohler, and P. Gunter, "Lithium niobate on insulator (LNOI) for micro-photonic devices," Laser Photon. Rev. **6**, 488–503 (2012).
11. H.-P. Chung, C.-H. Lee, K.-H. Huang, S.-L. Yang, K. Wang, A. S. Solntsev, A. A. Sukhorukov, F. Setzpfandt, and Y.-H. Chen, "Broadband on-chip polarization mode splitters in lithium niobate integrated adiabatic couplers," Opt. Express **27**, 1632–1645 (2019).
12. L. Zhou, X. Wang, L. Lu, and J. Chen, "Integrated optical delay lines: a review and perspective Invited," Chin. Opt. Lett. **16**, 101301 (2018).

13. M. Nishiura, Z. Yoshida, T. Mushiake, Y. Kawazura, R. Osawa, K. Fujinami, Y. Yano, H. Saitoh, M. Yamasaki, A. Kashyap, N. Takahashi, M. Nakatsuka, and A. Fukuyama, "Electro-optic probe measurements of electric fields in plasmas," Rev. Sci. Instrum. **88**, 023501 (2017).
14. I. Wilke, A. M. MacLeod, W. A. Gillespie, G. Berden, G. M. H. Knippels, and A. F. G. van der Meer, "Single-shot electron-beam bunch length measurements," Phys. Rev. Lett. **88**, 124801 (2002).
15. I. Saniour, G. Gaborit, A. L. Perrier, L. Gillette, G. Revillod, R. Sablong, L. Duvillaret, and O. Beuf, "Electro-optic probe for real-time assessments of RF electric field produced in an MRI scanner: feasibility tests at 3 and 4.7 T," NMR Biomed. **31**, e3849 (2018).
16. N. Council, D. Sciences, and C. Security, *Laser Radar: Progress and Opportunities in Active Electro-Optical Sensing* (National Academies, 2014).
17. K. Yang, T. Marshall, M. Forman, J. Hubert, L. Mirth, Z. Popović, L. P. Katehi, and J. F. Whitaker, "Active-amplifier-array diagnostics using high-resolution electrooptic field mapping," IEEE Trans. Microw. Theory Tech. **49**, 849–857 (2001).
18. K. Sarabandi, J. Choi, A. Sabet, and K. Sabet, "Pattern and gain characterization using nonintrusive very-near-field electro-optical measurements over arbitrary closed surfaces," IEEE Trans. Antennas Propag. **65**, 489–497 (2017).
19. E. D. Palik, *Handbook of Optical Constants of Solids* (Academic, 1998).
20. A. Rao and S. Fathpour, "Compact lithium niobate electrooptic modulators," IEEE J. Sel. Top. Quantum Electron. **24**, 1–14 (2018).
21. A. Rao, A. Patil, P. Rabiei, A. Honardoost, R. DeSalvo, A. Paolella, and S. Fathpour, "High-performance and linear thin-film lithium niobate Mach–Zehnder modulators on silicon up to 50 GHz," Opt. Lett. **41**, 5700–5703 (2016).
22. A. Rao, A. Patil, J. Chiles, M. Malinowski, S. Novak, K. Richardson, P. Rabiei, and S. Fathpour, "Heterogeneous microring and Mach-Zehnder modulators based on lithium niobate and chalcogenide glasses on silicon," Opt. Express **23**, 22746–22752 (2015).
23. C. Wang, M. Zhang, B. Stern, M. Lipson, and M. Loncar, "Nanophotonic lithium niobate electro-optic modulators," Opt. Express **26**, 1547–1555 (2018).
24. C. Wang, M. Zhang, X. Chen, M. Bertrand, A. Shams-Ansari, S. Chandrasekhar, P. Winzer, and M. Lončar, "Integrated lithium niobate electro-optic modulators operating at CMOS-compatible voltages," Nature **562**, 101–104 (2018).
25. J. Macario, P. Yao, S. Shi, A. Zablocki, C. Harrity, R. D. Martin, C. A. Schuetz, and D. W. Prather, "Full spectrum millimeter-wave modulation," Opt. Express **20**, 23623–23629 (2012).
26. A. J. Mercante, S. Shi, P. Yao, L. Xie, R. M. Weikle, and D. W. Prather, "Thin film lithium niobate electro-optic modulator with terahertz operating bandwidth," Opt. Express **26**, 14810–14816 (2018).
27. P. Rabiei, J. Ma, S. Khan, J. Chiles, and S. Fathpour, "Heterogeneous lithium niobate photonics on silicon substrates," Opt. Express **21**, 25573–25581 (2013).
28. R. N. Simons, *Coplanar Waveguide Circuits, Components, and Systems* (Wiley, 2001).
29. K. Luke, P. Kharel, C. Reimer, L. He, M. Loncar, and M. Zhang, "Wafer-scale low-loss lithium niobate photonic integrated circuits," Opt. Express **28**, 24452–24458 (2020).
30. D. H. Naghski, J. T. Boyd, H. E. Jackson, S. Sriram, S. A. Kingsley, and J. Latess, "An integrated photonic Mach-Zehnder interferometer with no electrodes for sensing electric fields," J. Lightwave Technol. **12**, 1092–1098 (1994).
31. ThorLabs, "Fiber paddle controllers: achieving distinct polarization states," https://www.thorlabs.com/images/TabImages/Fiber_Polarization_Controller_Lab_Facts.pdf.
32. B. Steffen, M. Czwalinna, C. Gerth, and P. Peier, "First electro-optical bunch length measurements from the European XFEL," in *7th International Beam Instrumentation Conference* (2019), pp. 338–341.